Run-to-Run Control of Inductively Coupled C2F6 Plasmas Etching of SiO2 : Construction of a Process Simulator with a CFD code

Seung T. Seo*, Yong H. Lee*, Kwang S. Lee*a, Dae R. Yang***, Bum Kyoo. Choi**

* Department of Chemical and Biological Engineering, Sogang University, Seoul, Korea
**Department of Mechanical Engineering, Sogang University, Seoul, Korea
***Department of Chemical and Biological Engineering, Korea University, Seoul, Korea

[a] Corresponding author: (Tel : +82-2-705-8477; E-mail: kslee@sogang.ac.kr)

Abstract: A numerical process to simulate SiO2 dry etching with inductively coupled C2F6 plasmas has been constructed using a commercial CFD code as a first step to design a run-to-run control system. The simulator was tuned to reasonably predict the reactive ion etching behavior and used to investigate the effects of plasma operating variables on the etch rate and uniformity. The relationship between the operating variables and the etching characteristics was mathematically modeled through linear regression for future run-to-run control system design.

Keywords: ICP etcher, C2F6 plasma, SiO2 etching, run-to-run control

1. INTRODUCTION

Plasma processing plays an important role in the micro-electronics fabrication. In the recent semi-conductor fabs, around one third of the manufacturing steps are known to be related to the plasma processing like dry etching, chemical vapor deposition, cleaning, and ashing. Among them, the dry etching is regarded as the trickiest application because of not only the complicated plasma behavior but also the poorly understood surface reactions. For this reason, the operating conditions for plasma etchers are usually found through time-consuming trial-and-error test runs. Such a difficulty may be overcome if we have a systematic and efficient way to search for the optimum operating condition. With the above problem in mind, the authors have conducted a research to develop a run-to-run control technique for SiO2 film etching in C2F6 inductively coupled plasma (ICP).

The ICP is generated by an RF current passing through a coil winding around a dielectric chamber. The RF current produces a magnetic field changing in upward and downward directions, which induces a circular electric field along which the electrons are forced to move while colliding with other gas particles in the chamber. This extends the number of collisions of an electron before it annihilates by neutralization on the chamber wall and enables higher density plasma than in the capacitively coupled plasma. Another advantage of the ICP etcher is that a separate RF power can be applied to the wafer chuck. The RF power develops a bias potential over the sheath through which ions are accelerated and bombard the wafer surface. In this way, the ion bombardment energy can be independently controlled by the chuck RF power while the plasma density can be adjusted by the chamber RF power [1].

In SiO2 etching, fluorocarbon plasmas are widely used due to the high etch rate and high selectivity over Si etching [2-4]. The fluorocarbon gas can be chosen among CF4, C2F6, and possibly other higher carbon content ones. By the collision with the high energy electrons, the gas is dissociated into different radicals and ions like F, CF_x, and CF_x^+. In typical ICP, less than a few percent of the feed gas is dissociated into the plasma components. It is known that the CF_x radicals tend to attach to the SiO2 surface making active monomer sites[5-7]. The active monomer sites are combined again with the CF_x radicals producing active polymer sites. These sites continue to grow and form passivation polymer layers on the SiO2 surface. The F/C ratio of the polymer layer is known to be around 1. On the other hand, the ions attack the SiO2 surface or the passivation layer with high bombardment energy etching the surface through reaction or by sputtering [8].Hence, two competitive reactions, polymer layer forming and etching, take place on the SiO2 surface. Which one dominates the other mainly depends on the ion bombardment energy and the F/C ratio of the feed gas. Fig. 1 shows an exemplary window for etching versus polymerization. For high bias voltage, *i.e.,* large ion bombardment energy, and high F/C gases, etching governs the surface reaction, and vice versa. In SiO2 etching, atomic or molecular oxygen is produced when fluorine radical reacts with SiO2. The oxygen is apt to combine with the carbon in CF_x radicals to form CO and CO2 and consequently, suppresses CF_x radicals from being involved in polymerization. In Si etching, however, no oxygen comes out and the polymer layer forming is not hindered by carbon depletion. This is why the fluorocarbon gases can have higher etching selectivity on SiO2 than Si.

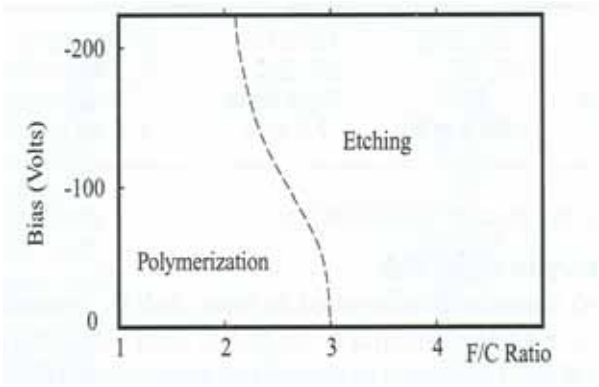

Fig. 1. Relationship between polymerization and Etching

In plasma etching, the etch rate and uniformity are two most important quality variables. They depend on ion flux and energy as well as neutral radical flux [9]. Among them, the ion energy can be manipulated by adjusting the bias voltage or equivalently, the RF power applied to the wafer chuck, whereas the ion and neutral fluxes are complex functions of chamber pressure, RF power, and gas flow rate. Therefore, determination of the operating variables for a desired etching state usually becomes a nontrivial task.

In this research, a numerical simulator has been developed for an ICP etcher for SiO2 etching with C2F6 plasmas using a commercial CFD code called CFD-ACE+/TOPO with the

final goal to develop a run-to-run control system of the etcher. The simulator will be used as a test plant as well as an underlying model from which the run-to-run controller is derived. The controller can be employed to improve the operation of real processes since run-to-run control can accommodate model uncertainty of roughly up to 100% without losing its ultimate performance [10]. To develop the simulator, we judiciously tuned the associated simulation modules in CFD-ACE+/TOPO by selecting appropriate reaction sets and adjusting kinetic parameters for the gas phase as well as surface reactions. Using the simulator, the effects of operating variables including RF power, bias voltage, chamber pressure, and gas flow rate on the etch rate and uniformity were investigated. Finally, a linear input-output model was derived for future run-to-run controller design.

2. ICP Etcher Model by CFD-ACE+

2.1. Process Description

The schematic diagram of the ICP etcher concerned in this study is given in Fig. 2. It has a multi-turn RF coil around the dielectric plasma chamber. The 13.56 MHz RF power is inductively coupled to the plasma by transformer action and the plasma acts as a single-turn lossy conductor. To the wafer chuck, a separate 13.56 MHz RF source is connected for independent adjustment of ion bombardment. The wafer temperature is controlled by a gas cooling system. The etcher has an axisymmetric shape and a 2-dimensinal model was considered to represent the process. In fact, the etcher model considered in this sturdy is a simplified model of the Multiplex plasma etcher from Surface Technology System Co.

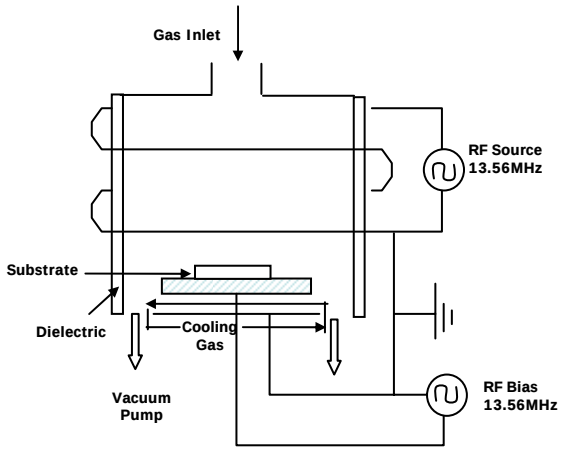

Fig. 2. Schematic diagram of the ICP etcher.

2.2. Governing Equations

The governing equations for the ICP etcher consist of mass, momentum, and enthalpy balances with appropriate boundary conditions for ionic and neutral species and also for electrons that comprise the plasmas. The balance equations are completed by necessary constitutive equations such as reaction equations in the bulk plasma as well as on the wafer surface, electro-magnetic relationships, thermodynamic and transport relationships, and so forth. In reality, rigorous description of all the above equations is formidable and solving them as a whole is impractical. Hence, simplification to a reasonable degree is necessary.

In the ICP etcher model in CFD-ACE+, neutrals, ions, and electrons are treated in different ways according to their unique respective characteristics. For neutrals consisting of gas molecules and radicals, mass and momentum balances for usual uncharged fluids are applied to each component.

For ions, external force by the electric field is included in the momentum balance. In addition, the component flux density in the mass balance is described by the following drift diffusion approximation:

$$\mathbf{J}_i = -\rho D_i \nabla y_i + \rho y_i \mathbf{u}_{di} + \mathbf{J}_c \tag{1}$$

where y, ρ, and D denote the mass fraction, mass density, and diffusion coefficient, respectively; $\mathbf{u}_d$ is the drift velocity given by

$$\mathbf{u}_{di} = \mathbf{E}\,(q_i \mu_i - \sum_j q_j \mu_j y_j) \tag{2}$$

where $\mathbf{E}$, q, and μ are electric field, charge, and mobility, respectively. $\mathbf{J}_c$ represents a bulk mass flux that appears to satisfy the mass conservation $\sum \mathbf{J}_i = 0$. The temperature of ions and neutrals are assumed to be same and described by a single enthalpy balance equation. In the enthalpy balance, Joule heating (or Ohmic heating) by the ion current in the electric field is considered together with the heat of reaction (energy gain or loss by collisions).

For electrons, the number density is obtained from the those of ions by the quasi-neutrality condition instead of solving the mass balance equation. Also the electron flux density is calculated by the following drift diffusion approximation instead of the solving the momentum balance equation:

$$\mathbf{J}_e = \mu_e n_e \mathbf{E} - D_e \nabla n_e \tag{3}$$

where n_e denotes the number density of electron. The energy balance is written in terms of the electron temperature T_e such that

$$\frac{3}{2}\frac{\partial}{\partial t}(n_e T_e) + \nabla \cdot \left(\frac{5}{2} T_e \mathbf{J}_e - \frac{5}{2} n_e D_e \nabla T_e \right) = -\mathbf{J}_e \cdot \mathbf{E} + P_{ext} - L \tag{4}$$

In the above, the energy flux consists of convection term $(5/2)T_e \mathbf{J}_e$ and thermo-diffusion term $(5/2) n_e D_e \nabla T_e$. $-\mathbf{J}_e \cdot \mathbf{E}$, P_{ext}, and L represent the joule heating absorbed by the electrons, the external power by collisionless heating, and the energy loss by reactions (or collisions), respectively.

In CFD-ACE+, the mass balance for the gas molecules and the momentum balances for the ions and neutrals are solved in the flow module; the mass balances for the ions and radicals are solved in the chemistry module; the enthalpy balances for the ions and neutrals are solved in the heat transfer module; and the enthalpy balance for the electron and the electron number density from the quasi-neutrality condition are solved in the plasma module. The plasma module also provides plasma specific constitutive terms required by other modules. The electric field is computed in the electric and magnetic modules according to

$$\mathbf{E} = -\nabla \varphi - \frac{\partial \mathbf{A}}{\partial t} \tag{5}$$

where φ and A denote the electrostatic and vector magnetic potentials, respectively, which are obtained by solving the Maxwell's equations in the frequency domain.

The surface as well as plasma reactions are specified in the chemistry module. Indeed this part is most crucial in determining the quality of the simulator. In the subsequent two sections, the reactions considered in this research are described for the bulk phase plasma, the wafer surface, and other walls.

2.3. Gas Phase Reactions

Due to its light mass, electrons are easily accelerated by the electric field while ions are not. The average electron energy reaches 2-7 eV in a typical ICP etcher, which roughly corresponds to 20,000-80,000K. On the other hand, the average ion energy is around 0.03-0.06eV or 350-700K. Under this non-thermal equilibrium state, the plasma reactions are governed by the collision of electrons with neutral and ionic species. Reactions between heavy particles are rare compared to the electron-impact reactions.

For an electron-impact reaction, the most fundamental information is the collision cross-section of the reaction. In Fig. 3, cross-sections for different electron-impact reactions are given for C2F6 gas as functions of the electron energy [11]. CFD-ACE+ is a continuum model-based program and the Arrhenius-type reaction rates are used instead of the cross-section data. However, CFD-ACE+ also accepts the cross-section data but converts to the Arrhenius-type reaction rate data internally assuming the Maxwellian energy distribution for the electrons [12]. In CHEMKIN, a commercial software for chemical reactor simulation, 132 gas phase plasma reactions with Arrhenius-type reaction rate data are provided for C2F6 plasmas by converting the Christophorou et al.'s data [13] and others. Since that number is too large to accommodate in the two-dimensional rigorous ICP etcher model, we selected 24 reactions that have direct effects on the SiO2 etching. For example, electron-impact reactions with SiFx gases that produce SiFy gases and F radical are omitted since F is known to have far less effect on SiO2 etching compared to CFx radicals and ions. Likewise, electron-impact reactions with oxygen and CO were not considered. In Table 1, the reaction set considered in this research is shown. Indeed, it is the whole collection of the electron-impact reactions of all possible CFx neutral and ionic components gathered in CHEMKIN.

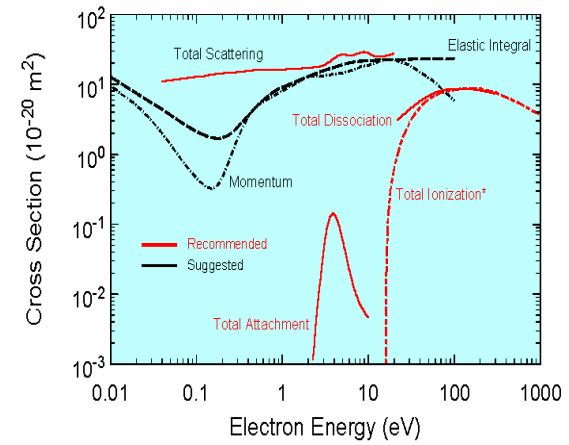

Fig. 3. Electron interaction cross-sections for C2F6 gas [11].

Table 1. Gas-phase reactions for C2F6 plasmas.

Ionization & Dissociation
C2F6 + e → 2CF3 + e
C2F6 + e → CF3 + CF3+ + 2e
C2F6 + e → CF2+ + CF4 + 2e
C2F6 + e → CF4 + CF+ + F + 2e
CF4 + e → CF3 + F + e
CF4 + e → CF3 + F+ + e
CF4 + e → CF2 + 2F + e
CF4 + e → CF3+ + F+2e
CF4 + e → CF3+ + F+ + 3e
CF4 + e → CF2+ + 2F + 2e
CF4 + e → CF2+ + F+ + F + 3e
CF3 + e → CF3+ + 2e
CF3 + e → CF2 + F + e
CF3 + e → CF2 + F+ + 2e
CF3 + e → CF2+ + F + 2e
CF3 + e → CF+ + 2F + 2e
CF2 + e → CF + F + e
CF2 + e → CF+ + F + 2e
CF2 + e → CF2+ + 2e
CF2 + e → CF + F+ + 2e
CF + e → CF+ + 2e
F + e → F+ + 2e
Recombination
CF2+ + e → CF + F
CF3+ + e → CF2 + F

2.4. Surface Reactions

The etching reactions on the SiO2 surface is more difficult to investigate than the bulk phase plasma reactions since adsorption, desorption, surface migration, etc. that are hard to observe individually and measure quantitatively occur along with the reactions on the surface. Nonetheless, intensive researches during the past decade have enabled us to comprehend the overview and some key features of the surface reactions.

It was mentioned that the fluorocarbon plasmas are subject to competitive reactions between polymerization and etching on the SiO2 film. The CF_x and F radicals isotropically diffuse to and stick on the oxide surface to form 'surface sites' as monomer-covered oxide ($SiO2CF_x^*$) and fluorinated oxide ($SiO2F2^*$). It is generally accepted that CF has the highest sticking tendency among CFx and F radicals [14]. The active sites are easily combined with incoming radicals and form a polymer passivation layer with F/C ratio of about one.

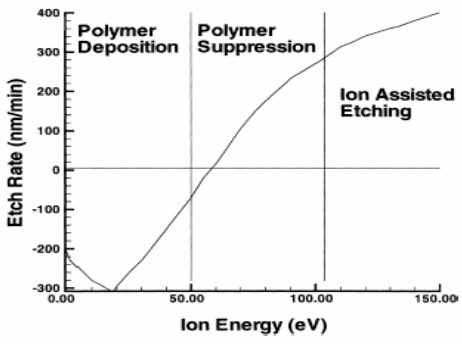

Fig. 4. Surface reactions (deposition to etching) with increasing ion energy [14].

Unlike the radicals, ions are accelerated by the electric field over the sheath and bombard the wafer surface in the vertical direction. The bombardment energy can be adjusted by the chuck bias voltage. Fig. 4 demonstrates how the dominant surface reaction varies with the ion energy. At low energy (< 50 eV), the ion bombardment cannot suppress the polymerization reaction. As the ion energy is increased, ion bombardment begins to overwhelm the polymerization by sputtering the polymer sites and removing the deposited polymer before it forms a continuous film [2]. At even higher ion energy, the ions are actively react with SiO2 together with other activated monomer site to produce the etch product SiF2 and SiF4 with byproducts like CO and CO2. The etching rate is known to be enhanced by the existence of activated monomer sites, hence the ion enhanced etching (RIE) is enabled. Fluorine atom can directly etch the SiO2 film but the contribution is not significant compared to the ion reactions.

Even with the above mentioned understanding, many features of the surface reactions still remain unveiled and quantitative description is still apart from the reality although the gap has been continuously reduced. In CFD-ACE+, the rate of the surface reaction is defined by the sticking coefficient. However, the sputtering yield is additionally considered in the ion enhanced reaction. For example, the rate of the radical reaction

$$F + 0.5\ SiO2^{*}(S) \rightarrow 0.5\ SiO2F2^{*}(S) \quad (6)$$

is expressed as Sc [F][$SiO2^{*}$(S)] where Sc, [F], and [$SiO2^{*}$(S)] represent the sticking coefficient, volume concentration of F and surface concentration of the activated SiO2 site, respectively. The rate of the ion enhanced reaction

$$CF2^{+} + ySiO2(B) + 2ySiO2F2^{*}(S) \rightarrow CF2 + yO2 + y\ SiF4 + 2ySiO2^{*}(S) \quad (7)$$

is expressed as Sc [$CF2^{+}$][$SiO2^{*}$(S)]. Together with this, the sputtering yield is given as

$$y = \max\left[a\left(\sqrt{E_i} - \sqrt{E_{th}}\right), 0 \right] \quad (8)$$

where E_i is the ion energy, and E_{th} is the threshold energy.

In this study, we relied on the reaction equations supplied in CHEMKIN and selected 20 equations out of 55 for possible simulation in a reasonable time span. The selected reactions are the ones by CFx and F ions and radicals while the rejected reactions are the ones by SiFx, CO, CO, O, and O2. The sticking coefficients were, however, partly modified so that the rate of the associated reactions complies with the experimental observations by different researchers as summarized in [5-7]. Since polymerization reactions are not contained in the CHEMKIN database, the simulation has been performed in the operating range where RIE prevails. On the side wall, electrons are consumed by recombination reactions. We considered eight reactions by referring to CHEMKIN and the work by Feldsien et al. [14]. In Table 2, surface reactions considered in this study are listed with respective sticking coefficients.

Indeed, the surface reactions are used to define the boundary conditions of the partial differential equations for the ICP model. For example, the boundary condition for the mass balance equation of species *i* is given by the following flux balance:

$$\mathbf{n} \cdot \mathbf{J}_i = S_i \quad (9)$$

where **n** is a unit normal vector to the surface and S_i is the surface production (or consumption) rate per unit area.

Table 2. Surface reactions and sticking coefficients.

Wafer	**S.C**
F+0.25SiO2(B)→0.25SiF4+0.25O2	0.15823
F^{+}+SiO2*(S)→F+SiO2*(S)	0.8
F+0.5SiO2*(S)→0.5SiO2F2*(S)	0.02
F^{+}+0.5SiO2*(S)→0.5SiO2F2*(S)	0.2
CF+SiO2* (S)→SiO2CF*(S)	0.66
CF^{+}+SiO2*(S)→CF+SiO2*(S)	0.8
F+0.5SiO2CF*(S)→0.5CF3+0.5SiO2*(S)	0.01
CF^{+}+SiO2*(S)→SiO2CF*(S)	0.2
$CF2^{+}$+SiO2*(S)→CF2+SiO2*(S)	0.8
$CF3^{+}$+SiO2*(S)→CF3+SiO2*(S)	0.8
$CF3^{+}$+SiO2(B)+2SiO2F2*(S)→CF3+SiF4+O2+2SiO2(S)	1
$CF2^{+}$+SiO2(B)+2SiO2F2*(S)→CF2+SiF4+O2+2SiO2(S)	1
CF^{+}+SiO2(B)+2SiO2F2*(S)→CF+SiF4+O2+2SiO2(S)	1
F^{+}+SiO2(B)+2SiO2F2*(S)→F+SiF4+O2+2SiO2(S)	1
$CF3^{+}$+SiO2(B)+2SiO2CF*(S)→CF3+SiF2+2CO+2SiO2*(S)	1
$CF2^{+}$+SiO2(B)+2SiO2CF*(S)→CF2+SiF2+2CO+2SiO2*(S)	1
CF^{+}+SiO2(B)+2SiO2CF*(S)→CF+SiF2+2CO+2SiO2*(S)	1
F^{+}+SiO2(B)+2SiO2CF*(S)→F+SiF2+2CO+2SiO2*(S)	1
CF2+1.5SiO2*(S)→SiO2CF*(S)+0.5SiO2F2*(S)	0.02
$CF2^{+}$+1.5SiO2*(S)→SiO2CF*(S)+0.5SiO2F2*(S)	0.2
Wall	
$CF3^{+}$+e→CF3	0.6
$CF3^{+}$+e→CF2+F	0.4
$CF2^{+}$+e→CF2	0.7
$CF2^{+}$+e→CF+F	0.28
CF^{+}+e→CF	1
F^{+}+e→F	1
2F+M→F2+M	0.5
2CF3→C2F6	0.01

2.5. Feature Scale Simulation

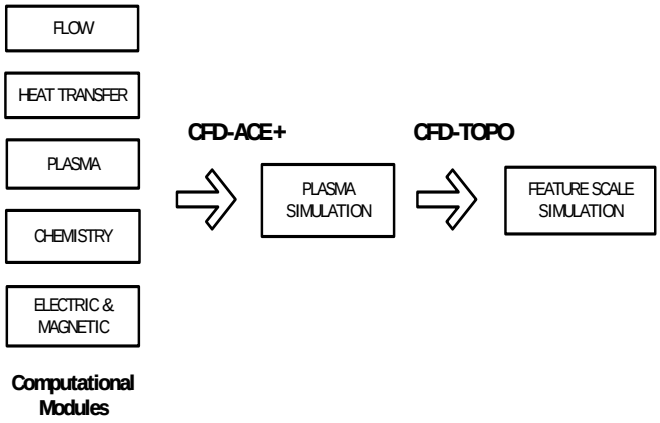

Fig. 5. CFD-ACE+/TOPO for multi-physics simulation.

Once CFD-ACE+ solves the ICP model, energy and angle of ion and radical fluxes on the wafer surface are obtained. CFD-TOPO takes this information to simulate the surface reactions and calculates the time-varying etching profile using the level set method. CFD-TOPO has no parameters to tune except the initial geometry of the photo-resist pattern on the SiO2 surface. Fig. 5 shows an overall structure of the ICP simulator by CFD-ACE+/TOPO.

3. SIMULATION STUDY

3.1. Chamber Geometry and Simulation Conditions

In Fig. 6, detailed geometry of the ICP chamber model is shown together with the wafer pattern for feature scale simulation. Here, the point designated as `probe' is the hypothetical position where plasma variables are measured. It is assumed that the RF coil is made of copper with radius of 0.6 cm and has five turns around the chamber wall. It is assumed that the temperature of the chamber wall is maintained at 300K. Also the wafer temperature is assumed to be regulated at 573K. The wafer pattern is assumed to be stripes with 250nm of opening. The photo resist is assumed to be completely intact by the plasmas.

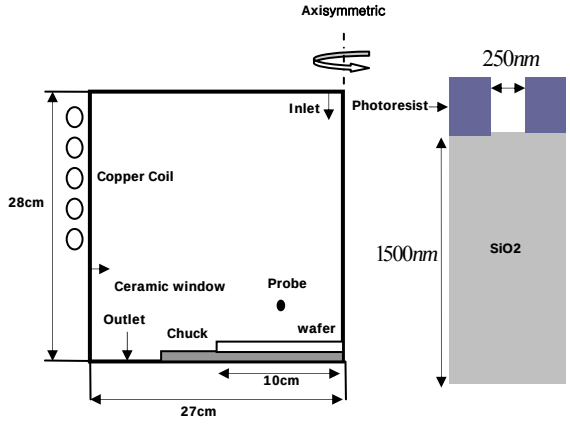

Fig. 6. Detailed geometry of ICP etcher and wafer pattern.

Table 3 shows the operating variables and their ranges considered in the simulation. The C2F6 flow rate was fixed at 50 sccm since its effect is less salient than other variables once it exceeds a certain value. Consequently, the chamber pressure, main RF power, and bias RF power were chosen as the operating variables. Also we took 2Kw, 10 mtorr, and 200 V as the base condition for the respective operating variables. By changing the variables around the base condition, the plasma as well as etching states were investigated and then a linear regression model between the operating variables and etching state was determined for run-to-run controller design.

Table 3. Operating variables and their ranges considered in the simulation.

Operating variable	Range
RF power (Kw)	1 - 3
Pressure (mtorr)	5 - 30
RF bias voltage (V)	150 - 300

3.2. Results and Discussion

Fig. 7 shows a profile of the electron number density in the chamber at the base condition. The simulator produced the maximum electron number density of $5.71 \times 10^{17} m^{-3}$ and average electron temperature of 3.38eV. These values well correspond to the results in typical ICPs [15]. Because the recombination reactions consuming electrons mainly occur on the side wall, the electron number density (END) is large at the core and decreases gradually along the outward direction.

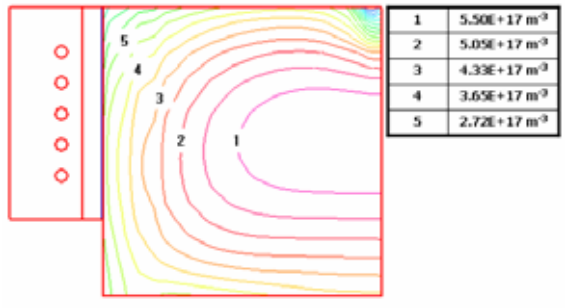

Fig. 7. Electron number density at 2Kw, 10mtorr, 200V bias.

Fig. 8 shows the effects of the RF power and chamber pressure on the END. The END increases with both RF power and pressure. Indeed this is an expected consequence because new electrons are produced in many plasma reactions as shown in Table 1 and thus increase in the collision rate necessarily results in a higher END. It is manifest that the collision rate increases as the RF power and chamber pressure increases by enhancing the electron energy and reducing the mean free path. Although it is not shown, the electron energy

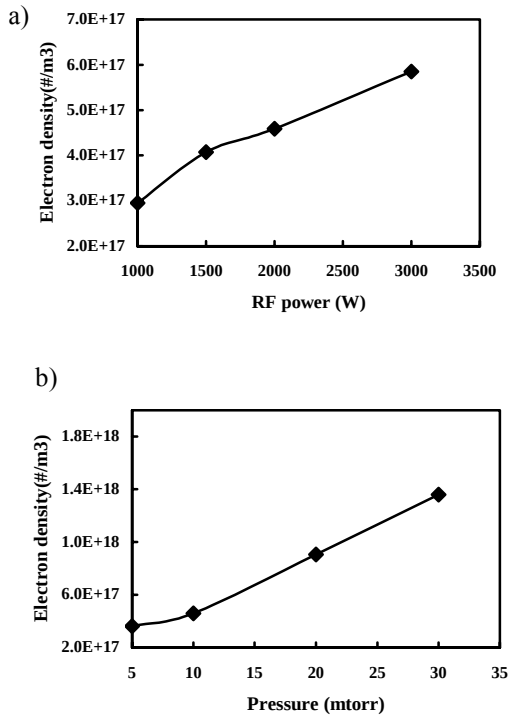

Fig. 8. Electron number density with RF power (a) and pressure (b) at the probe point (2Kw, 10mtorr, 200V RF bias).

decreases with the chamber pressure.

Fig. 9 shows an effect of RF bias on the etch rate through the feature scale simulation. At high bias, the etch rate increases due to high ion energy. Although it is not shown, the ion flux on the wafer increases when the RF power and pressure increase. Therefore, if the RF bias is high enough (>150eV), the etch rate increase with RF power and pressure.

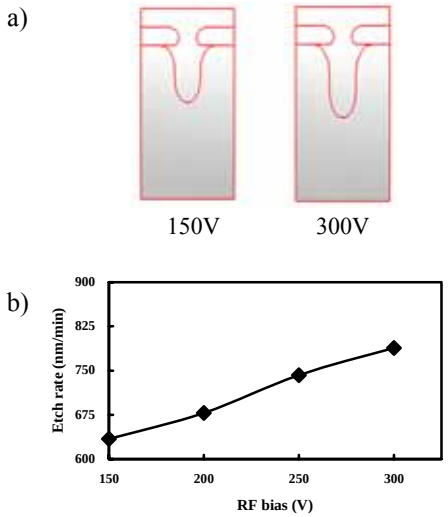

Fig. 9. Etch profiles (a) and etch rate (b) with RF bias on the wafer (2Kw, 10mtorr).

Fig. 10 shows how the etch rate uniformity varies with the change in the chamber pressure. Etch rates are monitored at five radial points on the wafer. As can be seen, the uniformity deteriorates as the pressure increases. Though not shown here, it was found that the RF power and RF bias do not sensitively affect the uniformity.

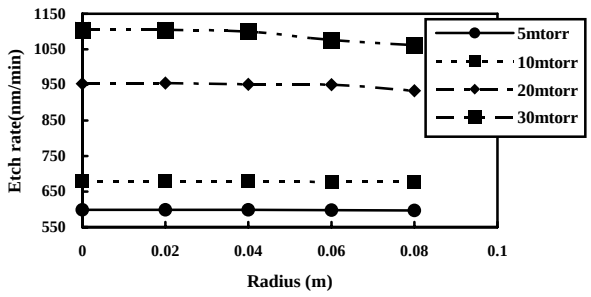

Fig. 10. The etch rate at wafer radius changing Pressure (2Kw, 200V RF bias).

3.3. Linear Modeling

For future run-to-run controller design, a linear static model that relates the operating variables and the etch rate and uniformity was determined through linear regression. The etch rate was defined as the average value and the uniformity was defined as the normalized standard deviation over the five monitoring points such that

$$X = (x1 + x2 + x3 + x4 + x5)/5 \quad \text{(nm)} \tag{10}$$

$$NU(\%) = \frac{\sigma}{X} \times 100 \tag{11}$$

where x and σ denote the etch rate and standard deviation, respectively. Eq (12) shows the resulting regression model.

$$\begin{bmatrix} X\ (\text{nm}) \\ NU\ (\%) \end{bmatrix} = \begin{bmatrix} 193.3632 & 20.1555 & 1.3352 \\ -0.3232 & 0.0460 & -0.0015 \end{bmatrix} \begin{bmatrix} U1\ (\text{Kw}) \\ U2\ (\text{mtorr}) \\ U3\ (\text{V}) \end{bmatrix} + \begin{bmatrix} -195.1989 \\ 1.2464 \end{bmatrix} \tag{12}$$

4. CONCLUSIONS

A numerical process to simulate SiO2 etching with C2F6 plasmas has been developed using CFD-ACE+/TOPO. It has been numerically confirmed that the etch rate and uniformity depend on the ion flux and energy. The ion flux is observed to be affected by the RF power and chamber pressure, and the ion energy was shown to be most strongly influenced by the RF bias. The relationship between operating variables and the etching state have been modeled through linear regression for construction of a run-to-run control system.

ACKNOWLEDGMENT

This work was supported by grant No. R01 – 2002 – 000 – 00574 - 0 from the Basic Research Program of the Korea Science & Engineering Foundation.

REFERENCES

[1] M. A. Lieberman and A. J. Lichtenberg, *Principles of Plasma Discharges and Materials Processing*, John Wiley & Sons, 1994.

[2] G. S. Oehrlein, Y. Zhang, D. Vender and O. Joubert, *J. Vac. Sci. Technol. A*, Vol. 12, No. 2, pp. 333-344, 1994.

[3] Hong Xiao, *Introduction to Semiconductor Manufacturing Technology*, Prentice Hall, 2001.

[4] L. Rolland, M.C. Peignon, Ch. Cardinaud and G. Turban, *Microelectronic Eng*, Vol. 53, pp. 375-379, 2000.

[5] J. P. Booth, G.. Hancock. N. D. Perry and M. J. Toogood, *J. Appl. Phys*, Vol. 66, No. 11, pp. 5251-5257, 1989.

[6] A. D. Tserepi, J. Derouard, J. P. Booth and N. Sadeghi, *J. Appl. Phys*, Vol. 81, No. 5, pp. 2124-2130, 1997.

[7] J.W. Thomas, J. R. Suzuki, S. H. Kable and J. I. Steinfeld, *J. Appl. phys*, Vol. 60, No. 8, pp. 2775-2777, 1986.

[8] K. Ninomiya, K. Suzuki, S. Nishimatsu and O. Okada, *J. Vac. Sci. Technol. A*, Vol. 58, No. 3, pp. 1177-1182, 1985.

[9] D. C. Gray, I. Tepermeister and H. H. Sawin, *J. Vac. Sci. Techno.l B*, Vol. 11, No. 4, pp. 1243-1257, 1993.

[10] W. C. Kim, In Sik. Chin, K. S. Lee and J. H. Choi, *Computers & Chemical Engineering*, Vol. 24, No. 8, pp. 1815-1819, 2000.

[11] NIST : Electricity Division, Electronics and Electrical Engineering Lab. [Online]. Available : http://www.eeel.nist.gov/811/refdata/c2f6/c2f6.html

[12] E. Meeks and P. Ho, *Thin Solid Film*, Vol. 365, pp. 334-347, 2000.

[13] L. G.. Christophorou, J. K. Olthoff and M. V. Rao, *J. Phys. Chem*, Ref. Data 27, 1998.

[14] J. Feldsien, D. S. Kim and D. J. Economou, *Thin Solid Films*, Vol. 374, pp. 311-325, 2000.

[15] Y. B. Hahn and S. J. Pearton, *kor. J. Chem. Eng*, Vol. 17, No. 3, pp. 304-309, 2000.